Chemical Science

ROYAL SOCIETY OF CHEMISTRY

EDGE ARTICLE

View Article Online
View Journal | View Issue



Cite this: *Chem. Sci.*, 2024, **15**, 11374

All publication charges for this article have been paid for by the Royal Society of Chemistry

Received 8th February 2024
Accepted 13th June 2024

DOI: 10.1039/d4sc00954a

rsc.li/chemical-science



# Chiral three-dimensional organic–inorganic lead iodide hybrid semiconductors†

Chang-Chun Fan, [ab] Cheng-Dong Liu, [b] Bei-Dou Liang, [b] Tong-Yu Ju, [b] Wei Wang, [b] Ming-Liang Jin, [b] Chao-Yang Chai [b] and Wen Zhang *[b]

Chiral hybrid metal halides (CHMHs) have received a considerable amount of attention in chiroptoelectronics, spintronics, and ferroelectrics due to their superior optoelectrical properties and structural flexibility. Owing to limitations in synthesis, the theoretical prediction of room-temperature stable chiral three-dimensional (3D) $CHFClNH_3PbI_3$ has not been successfully prepared, and the optoelectronic properties of such structures cannot be studied. Herein, we have successfully constructed two pairs of chiral 3D lead iodide hybrids (*R*/*S*/*Rac*-3AEP)$Pb_2I_6$ (**3*R*/*S*/*Rac***, 3AEP = 3-(1-aminoethyl)pyridin-1-ium) and (*R*/*S*/*Rac*-2AEP)$Pb_2I_6$ (**2*R*/*S*/*Rac***, 2AEP = 2-(1-aminoethyl)pyridin-1-ium) through chiral introduction and *ortho* substitution strategies, and obtained bulk single crystals of **3*R*/*S*/*Rac***. The **3*R*/*S*** exhibits optical activity and bulk photovoltaic effect induced by chirality. The **3*R*** crystal device exhibits stable circularly polarized light performance at 565 nm with a maximum anisotropy factor of 0.07, responsivity of 0.25 A $W^{-1}$, and detectivity of $3.4 \times 10^{12}$ jones. This study provides new insights into the synthesis of chiral 3D lead halide hybrids and the development of chiral electronic devices.

## Introduction

Chirality is one of the most essential characteristics in living organisms and nature universally,[1,2] and is necessary for complex biometric recognition and replication functions in living systems.[3] An object is chiral when its mirror image cannot be superimposed with the original object.[4,5] In materials science, chirality is often used to represent an important non-centrosymmetric structural feature that can be obtained by introducing chiral molecules.[6] The introduction of chirality usually brings optical rotation,[7] circular dichroism (CD),[8] and circularly polarized light (CPL) emission[4,9] in materials. In some cases, it can even induce non-centrosymmetry-related properties such as the bulk photovoltaic effect (BPVE),[10–12] second-harmonic generation,[13–15] piezoelectricity,[16,17] ferroelectricity,[18–20] Rashba splitting,[21,22] and topological quantum properties.[23] Although organic chiral materials exhibiting strong chiral activity in the near-ultraviolet region are widely available, the charge transfer capability of actual polarized optoelectronic devices is poor,[5] and there is an urgent need to develop new chiral lead iodide hybrids with strong absorption capacity and a broad light spectrum.

Metal halide hybrids, especially three-dimensional (3D) lead halide hybrids, have attracted great attention from researchers due to their excellent properties such as long carrier diffusion lengths,[24–27] high carrier mobility,[28,29] bandgap tunability,[30] low trap densities,[31] and high power conversion efficiency.[32] The continuous breakthrough of the record photoelectric conversion record efficiency of single-junction lead halide hybrid solar cells has completely triggered the research boom of lead halide hybrid semiconductor materials.[32] In addition, the structural diversity of organic cations in metal halides and the ionic properties of the inorganic framework make it possible to directly obtain chiral metal halides by introducing chiral cations. The introduction of chirality extends the excellent optoelectronic properties of metal halides to the field of chiral electronics, greatly expanding their application range and potential.[4,33–35] Tang *et al.* reported a CPL detector based on a 1D (*R*/*S*-PEA)$PbI_3$ (PEA = phenethylammonium) structure, providing an effective method for the direct detection of CPL.[36] In 2019, Xiong *et al.* reported a pair of 2D chiral metal halide ferroelectrics (*R*/*S*-CMBA)$_2PbI_4$ (CMBA = 1-(4-chlorophenyl) ethylammonium).[16] In 2020, Fu *et al.* reported the chiral ferroelectric (*R*/*S*-3-FPRD)$MnBr_3$ (3-FPRD = 3-fluoropyrrolidinium) with CPL emission properties; the luminescence asymmetry factor $|g_{lum}|$ is $6.1 \times 10^{-3}$, and the photoluminescence quantum yield is 28.31%.[37] Recently, Luo *et al.* constructed a pair of 3D chiral lead chloride hybrids (*R*/*S*-BPEA)$EA_6Pb_4Cl_{15}$ (BPEA = 1-4-bromophenylethylammonium, EA = ethylammonium),[38] but due to the large cavity of their inorganic framework, their band gap is much larger than that of the reported 3D lead iodide

[a]*College of Materials Engineering, Jinling Institute of Technology, Nanjing 211169, China*

[b]*Jiangsu Key Laboratory for Science and Applications of Molecular Ferroelectrics, School of Chemistry and Chemical Engineering, Southeast University, Nanjing 211189, China. E-mail: zhangwen@seu.edu.cn*

† Electronic supplementary information (ESI) available: Experimental details, Fig. S1–S15 and Tables S1–S5. CCDC 2323588–2323597. For ESI and crystallographic data in CIF or other electronic format see DOI: https://doi.org/10.1039/d4sc00954a

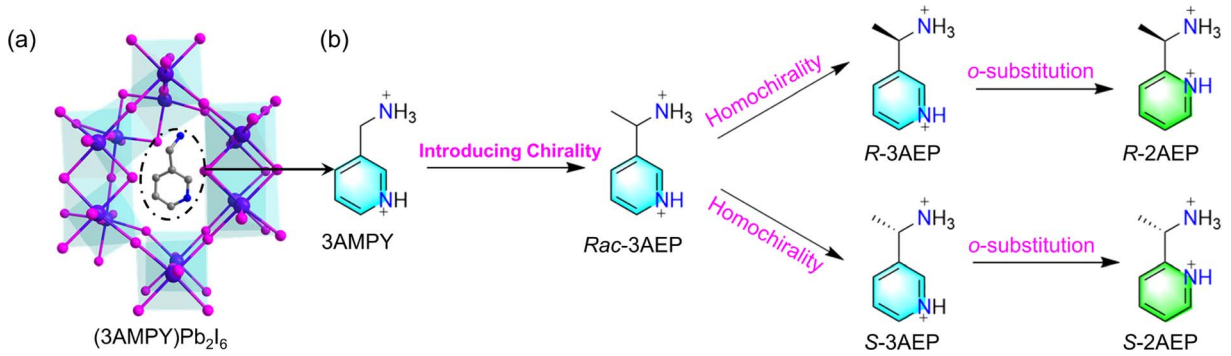


Scheme 1 (a) Crystal structure of (3AMPY)$Pb_2I_6$. (b) Molecular design for 3D chiral lead iodide hybrids.

hybrids.[39–41] However, until now, the chiral 3D lead iodide hybrids, which are theoretically predicted to be both thermodynamically and kinetically stable, have been rarely reported.[2]

Inspired by the organic-to-inorganic structural chirality transfer effect in chiral hybrid metal halides (CHMHs), we know that the introduction of chiral cations into the inorganic framework is the most direct and effective way to obtain CHMHs.[5] Here, using the 3D lead iodide hybrid (3AMPY)$Pb_2I_6$ (3AMPY = 3-aminomethylpyridinium) as a template and introducing methyl and *ortho* substitution strategies in the divalent cation 3AMPY (Scheme 1a and b), two pairs of 3D chiral lead iodide hybrids (*R*/*S*-3AEP)$Pb_2I_6$ (**3*R*/*S*/*Rac***, 3AEP = 3-(1-aminoethyl)pyridin-1-ium) and (*R*/*S*-2-AEP)$Pb_2I_6$ (**2*R*/*S*/*Rac***, 2AEP = 2-(1-aminoethyl)pyridin-1-ium) were synthesized, and bulk single crystals of **3*R*/*S*/*Rac*** were obtained. We find the BPVE under white-light irradiation in **3*R*/*S***. The sign of zero-bias photocurrent is altered depending on the configuration of the chirality *R*/*S*-3AEP. **3*R*/*S*** also exhibits chiroptical properties and the Rashba effect with a Rashba coefficient ($\alpha_R$) of 0.23 eV Å.

## Results and discussion

### Synthesis

We first referred to the synthesis method of (3AMPY)$Pb_2I_6$ reported in the literature (Fig. 1a)[39] and tried to use a 4 : 1 ratio of $Pb^{2+}$ to the 3-AMPY starting material to obtain the chiral 3D metal halide hybrids. However, we did not obtain the desired 3D structure, but only a 2D structure under this condition. We guessed that the introduction of the methyl group may increase the steric hindrance, leading to an increase in the synthesized energy barrier. This may be overcome by increasing the proportion of $Pb^{2+}$. We then investigated the 5 : 1, 6 : 1, and 7 : 1 ratios of $Pb^{2+}$ and the organic cation (Fig. 1b and c), and found that 3D structures can be obtained at 6 : 1 and higher ratios (Fig. 1c). However, a similar 3D lead iodide hybrid ($M_2$pda)$Pb_2I_6$ ($M_2$pda = *N*-methyl-1,3-propanediammonium) was found to be synthesized with a 3 : 1 ratio of starting materials,[41] which inspired us that reaction conditions play an important role in the structural dimensions of metal halides, especially the proportion of starting materials and reaction temperature.

Two pairs of chiral 3D lead iodide compounds **2*R*/*S*/*Rac*** and **3*R*/*S*/*Rac*** were thus synthesized with bivalent chiral cations as shown in Scheme 1b and Fig. S1.† Red block single crystals of **3*R*/*S*/*Rac*** with a size of 5 × 3 × 3.0 $mm^3$ were obtained by slowly evaporating the solutions at 80 °C (Fig. 1c and S2†). However, due to the solubility of **2*R*/*S*/*Rac*** and growth temperature constraints, a pure phase cannot be obtained, so the structures and properties of **3*R*/*S*/*Rac*** are studied below.

The purity of the phase was confirmed by powder X-ray diffraction (Fig. S3†). The infrared spectrum of the compounds shows several vibrational peaks at 1480, 3000, and 3500 $cm^{-1}$, which are attributed to the vibration absorption of N–H, C–H, C=C, and C=N bonds, respectively, demonstrating the successful introduction of the *Rac*/*R*/*S*-3AEP divalent cation into the 3D inorganic lattices (Fig. S4†). Thermogravimetric analysis shows the thermal stability of **3*R*/*S*/*Rac*** up to about 575 K (Fig. S5†), comparable to that of ($M_2$pda)$Pb_2I_6$ [41]and (Dmpz)$Pb_2I_6$.[40]

### Crystal structure

Single-crystal XRD analysis shows that **3*Rac*** crystallizes in the centrosymmetric space group *Cmca*, with cell parameters $a$ = 12.9279(4) Å, $b$ = 18.7439(6) Å, $c$ = 17.6358(5) Å, and $\alpha = \beta = \gamma$ = 90° (Table 1). In the **3*Rac*** structure, a mirror passes through the cation to result in a static disorder of the substituents of the pyridine ring (Fig. S6† and 1b). Due to the existence of the structural phase transition in **3*R*/*S***, we first analyze the structural characteristics of the low-temperature ordered state. Compounds **3*S*** and **3*R*** are all crystallized in the chiral space group $C222_1$ at 240 K with the cell parameters of $a$ = 12.9335(5) Å, $b$ = 18.7439(8) Å, $c$ = 17.6358(8) Å, and $\alpha = \beta = \gamma$ = 90° (Table 1). Due to the introduction of enantiomerically chiral cations, the crystal packing structures of the **3*S*** and **3*R*** exhibit mirror symmetry (Fig. 1e and f). To our knowledge, this is the first report of chiral 3D hybrid lead halides formed from lead halide octahedral dimers (Table S1†). The structure of **2*R*/*S*/*Rac*** adopts the same space group as **3*R*/*S*/*Rac*** (Table 1).

The basic structural motif of (AEP)$Pb_2I_6$ adopts a rare 3D lead iodide anion framework of $AM_2I_6$, where A is the bulky cation template for the inorganic lead iodide framework. The crystal structure contains 3D inorganic lead iodide inorganic frameworks of corner- and edge-sharing $PbI_6$ octahedra with vacancies occupied by the 3AEP organic cations. Four edge-sharing dimers are connected by the corners of the individual layers to

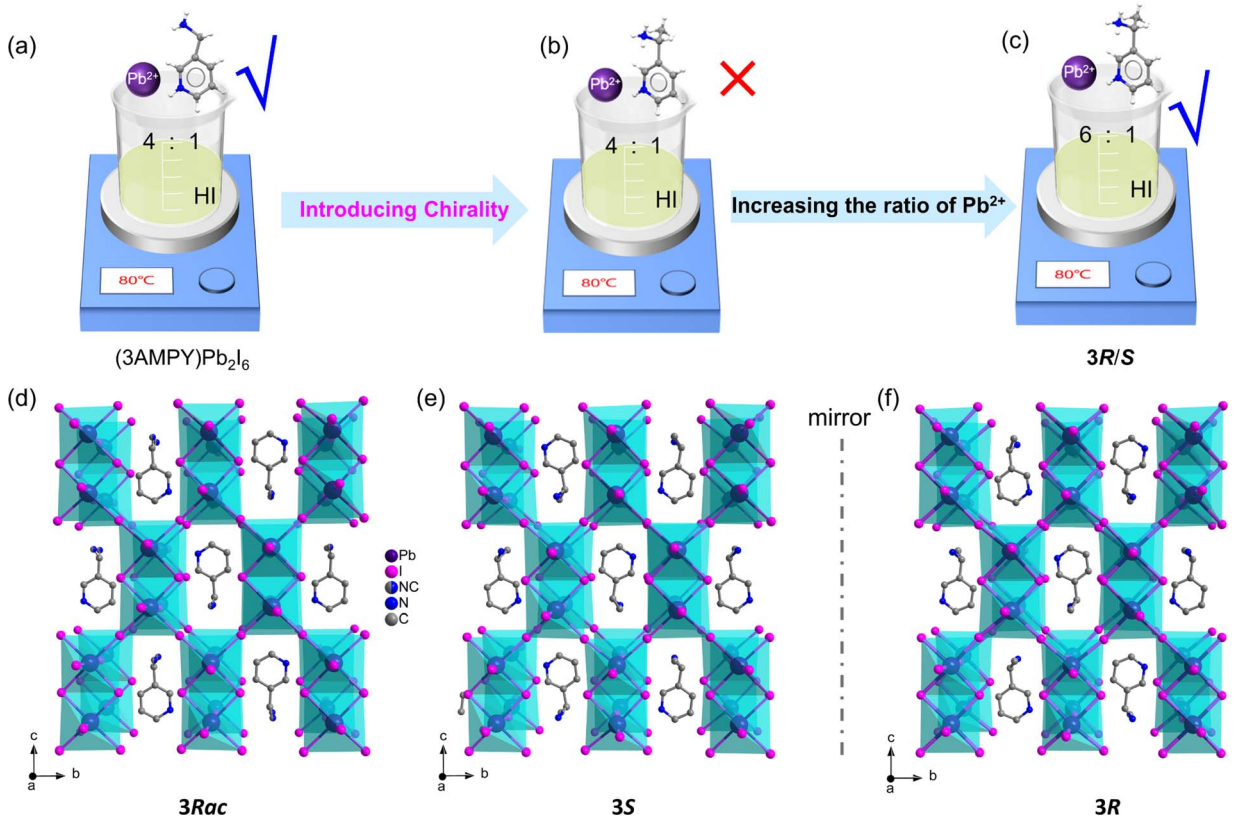


Fig. 1 (a) Synthesis of (3AMPY)$Pb_2I_6$. (b and c) Synthesis of 3*R*/*S*. Crystal structures of (d) 3*Rac*, (e) 3*S*, and (f) 3*R*.

form a continuous layer with rectangular voids extending along the *bc* crystal plane. The layers are stacked along the *a*-axis by angle-to-angle connections to form an anionic 3D inorganic framework (Fig. 1c and S7†). The rectangular void in the inorganic skeleton differs from the parallelogram void induced by the chain alkyl diamine in the $(M_2pda)Pb_2I_6$,[41] which is caused by the template effect of the characteristic size and rigid shape of 3AEP. The asymmetric unit consists of one 3AEP divalent cation, two Pb ions, and six I ions (Fig. S8a†). The 3AEP cations are located in the plane of the layer, perpendicular to the stacking direction in the pores. They are bonded to the 3D inorganic framework by the hydrogen bond interaction of N–H···I and C–H···I, with the bond lengths of N–H···I ranging from 2.85 to 3.2 Å and C–H···I ranging from 3.93 to 4.16 Å (Fig. S8b and c†). Hirshfeld surface analysis reveals a predominant role of the hydrogen bonding interactions of H···I and additional van der Waals interactions of C···I between the cations and the I anions (Fig. S9†). Rich hydrogen bonding and van der Waals interactions promote effective chiral transfer of the chiral cations to the inorganic sublattices, with $2_1$ screw axes crossing the corner-sharing octahedral bridging iodine atoms and twisted Pb–I planes along the *a* and *c* directions, respectively (Fig. S8d and Table S2†).

### Structural phase transition properties

Structural properties were analyzed in detail by taking **3*R*** as an example. The thermal properties of **3*R*** during the structural phase transition were investigated. As shown in Fig. 2a, **3*R*** exhibited two pairs of obvious endothermic and exothermic peaks at 293/275 K ($T_1$) and 419/414 K ($T_2$), indicating two reversible structural phase transitions. For the convenience of analysis, the phase below $T_1$ is referred to as the low temperature phase (LTP), the phase between $T_1$ and $T_2$ as the intermediate temperature phase (ITP), and the phase above $T_2$ as the high-temperature phase (HTP). At $T_1$, there is a thermal hysteresis of 18 K with a phase transition centered at 284 K, while at $T_2$ the thermal hysteresis is only 5 K with a phase transition center of 417 K. The $\Delta H$ at $T_1$ is 5.88 kJ mol$^{-1}$ and that at $T_2$ is 0.71 kJ mol$^{-1}$. As can be seen from Fig. 2b, **3*Rac*** does not undergo any structural phase transition in the corresponding temperature range. The temperature-dependent dielectric constant of **3*R*** crystalline powder was measured. As shown in Fig. 2c, the dielectric anomalies occur in the process of temperature change at different test frequencies. An obvious step-type dielectric anomaly can be seen from the 1 MHz curve, which confirms the DSC test results (Fig. 2a).

When the temperature increased to 298 K, the compound underwent an order–disorder phase transition due to the disordered substituents on the pyridine ring. The ordered and disordered cationic terminal groups did not cause changes in the space group (cell parameters, $a = 12.9629(5)$ Å, $b = 18.7955(5)$ Å, $c = 17.6714(8)$ Å, $\alpha = \beta = \gamma = 90°$) (Tables S3 and S4†). However, the bond length and bond angle of the inorganic anion skeleton are extended and enlarged with increasing temperature, which is a typical effect of thermal expansion and contraction. With the further increase of temperature to 425 K, the whole cations in the

Table 1 Crystal and refinement data for compounds reported here

| Compound | (*R*-3AEP)$Pb_2I_6$ | (*S*-3AEP)$Pb_2I_6$ | (*Rac*-3AEP)$Pb_2I_6$ |
|---|---|---|---|
| Formula | $C_7H_{12}N_2Pb_2I_6$ | $C_7H_{12}N_2Pb_2I_6$ | $C_7H_{12}N_2Pb_2I_6$ |
| Formula weight | 1299.97 | 1299.97 | 1299.97 |
| Crystal system | Orthorhombic | Orthorhombic | Orthorhombic |
| Space group | $C222_1$ | $C222_1$ | *Cmca* |
| *a*/Å | 12.9493(3) | 12.9335(5) | 12.9279(4) |
| *b*/Å | 18.7108(5) | 18.7439(8) | 18.7521(6) |
| *c*/Å | 17.6439(5) | 17.6358(8) | 17.6600(5) |
| *α*, *β*, *γ*/° | 90 | 90 | 90 |
| *V*/Å$^3$ | 4274.97(19) | 4273.3(3) | 4281.20(2) |
| Flack parameter | −0.016(16) | 0.00(3) | — |
| $R_{int}$ | 0.038 | 0.066 | 0.083 |
| $R_1$[a]/w$R_2$[b] ($I > 2\sigma(I)$) | 0.0606, 0.1713 | 0.0684, 0.1748 | 0.0561, 0.1520 |
| $R_1$/w$R_2$ (all data) | 0.0692, 0.1785 | 0.0900, 0.1865 | 0.0667, 0.1619 |
| GOF | 1.064 | 1.02 | 1.036 |
| Compound | (*R*-2AEP)$Pb_2I_6$ | (*S*-2AEP)$Pb_2I_6$ | (*Rac*-2AEP)$Pb_2I_6$ |
| Formula | $C_7H_{12}N_2Pb_2I_6$ | $C_7H_{12}N_2Pb_2I_6$ | $C_7H_{12}N_2Pb_2I_6$ |
| Formula weight | 1299.97 | 1299.97 | 1299.97 |
| Crystal system | Orthorhombic | Orthorhombic | Orthorhombic |
| Space group | $C222_1$ | $C222_1$ | *Cmca* |
| *a*/Å | 12.9873(5) | 12.9972(3) | 12.9548(6) |
| *b*/Å | 18.8387(7) | 18.8397(7) | 18.8648(9) |
| *c*/Å | 17.5741(8) | 17.5687(6) | 17.6101(7) |
| *α*, *β*, *γ*/° | 90 | 90 | 90 |
| *V*/Å$^3$ | 4299.7(3) | 4301.9(2) | 4303.7(3) |
| Flack parameter | 0.006(8) | 0.002(15) | — |
| $R_{int}$ | 0.0289 | 0.0593 | 0.0394 |
| $R_1$[a]/w$R_2$[b] ($I > 2\sigma(I)$) | 0.0286, 0.0593 | 0.0681, 0.1653 | 0.0517, 0.1058 |
| $R_1$/w$R_2$ (all data) | 0.0361, 0.0612 | 0.0856, 0.1807 | 0.0762, 0.1151 |
| GOF | 0.974 | 1.005 | 1.107 |

[a] $R_1 = \Sigma||F_o| - |F_c||/|F_o|$. [b] $wR_2 = [\Sigma w(F_o^2 - F_c^2)^2]/\Sigma w(F_o^2)^2]^{1/2}$.

inorganic framework undergo a violent disorder, causing the space group to change to *C*222 with higher symmetry (cell parameters, $a = 9.4786(5)$ Å, $b = 17.723(10)$ Å, $c = 6.5033(8)$ Å, and $\alpha = \beta = \gamma = 90°$) (Tables S3 and S4†). In the HTP, there are three mutually perpendicular 2-fold axes passing through the 3-AEP cation (Fig. S10†), corresponding to the highly disordered state. The bond lengths and bond angles of the inorganic skeleton have further lengthened and become larger (Fig. 2e, g and i). The Pb–I–Pb bond angles belonging to the canonical angle shared bond have not yet reached the standard 180° (Table S5†), and there are still tiny distortions in the structure (Fig. 2i).

## Semiconducting properties and the BPVE

DFT calculations were performed based on the 240 K crystal structure of **3*R*** using the exchange–correlation functional PBE (Fig. 3a and b). Both the valence and conduction bands exhibit dispersion, but the degree of dispersion is smaller than that of $CH_3NH_3PbI_3$ due to the relatively lower octahedral edge-sharing connectivity in the structure.[42] The data show that **3*R*** is a direct bandgap semiconductor with a bandgap value of 2.04 eV at the *Y*-point without spin–orbit coupling (SOC) (Fig. 3a), and turns to an indirect one with a bandgap value of 1.48 eV due to the Rashba spin splitting effect (Fig. 3b). Our PBE density of states (DOS) data show that Pb 6s and I 5p orbitals overlap to form the valence band maximum (VBM), and Pb 6p orbitals overlap to form the conduction band minimum (CBM), indicating that the energy band and semiconductor performance are mainly determined by the inorganic components (Fig. 3b). We find electronic states derived from the molecular sublattice ∼ 0.4 eV above the conduction band minimum. Higher accuracy electronic-structure approaches such as hybrid functionals or many-body perturbation theory and the inclusion of thermal broadening effects might lead to the participation of these molecular electronic states in the conduction band edge. Ultraviolet-visible diffuse-reflectance spectra of **3*R***, **3*S***, and **3*Rac*** are shown in Fig. 3c. There is significant absorption in the ultraviolet region, and the edge of the band extends into the visible light region near 600 nm. Based on the Kubelka–Munk equation,[43,44] the optical bandgap value is estimated to be 2.13 eV (Fig. 3a), which is smaller than the bandgap of common 2D lead iodide semiconductor materials,[45] and is comparable to that of chiral quasi-2D lead iodide hybrid (*R*/*S*-MPA)$_2$(MA)$Pb_2I_7$ (MA = methylammonium, MPA = methylphenethylammonium) (∼2.08 eV).[10]

The dark current and on/off ratio are the two main parameters that affect the optoelectronic properties of semiconductors. The dark current of the **3*R*** single crystal device along the [100] direction in a dark environment is as low as $10^{-10}$ A (Fig. 3d and e), which is much lower than $10^{-7}$ A of $MAPbI_3$.[46] Under sunlight irradiation of 100 mW cm$^{-2}$, the photocurrent rapidly increases to $3.6 \times 10^{-7}$ A, and the on/off ratio is greater than $4 \times 10^3$, consistent with our previously reported results.[41] The BPVE induced by chirality was observed in the *I*–*V* curve for the [001] parallel alignment with a zero-bias photocurrent with a short-circuit current $|I_{sc}|$ of ∼0.37 nA and an open-circuit voltage $|V_{oc}|$ of ∼0.11 V for both **3*R*** and **3*S*** (Fig. 3f). The $I_{sc}$ and $V_{oc}$ values are larger than those of reported quasi-2D CHMHs and (*R*/*S*-MPA)$_2$(MA)$Pb_2I_7$.[10] No BPVE phenomenon was observed in **3*Rac*** (Fig. 3f).

## Chiroptical properties and the Rashba–Dresselhaus effect

The CD spectra of **3*R*** and **3*S*** were measured on the crystal powders. In the wavelength range of 200–580 nm, there is a clear CD signal at the edge of the absorption band and exciton peak at 565 nm, extending to 580 nm. The enantiomers show the same signal size but an opposite sign of the absorption peaks at 565 nm, a typical Cotton effect in the CD spectrum (Fig. 4a). In contrast, **3*Rac*** has no characteristic absorption in the CD spectrum (Fig. 4a). At the same time, the UV-vis absorption spectra in the 200–580 nm range are consistent with the characteristic peaks of the CD absorption spectra (Fig. 3b). These results confirm the effective chiral transfer from the chiral cations to the inorganic sublattices. The calculated $g_{CD}$ is $4.1 \times 10^{-6}$ at 565 nm (Fig. 4b). Based on a **3*R*** single crystal device (Fig. 4c), we investigated its response to 565 nm CPL. The anisotropy factor for photocurrent ($g_{Iph}$) is up to 0.08 at a bias of 5 V and at 0.17 mW cm$^{-2}$ (Fig. 4d). This is smaller than the reported low-dimensional CHMH detector $g_{Iph}$,[22,36,47] and we speculate that is caused by the order–disorder motion of the cations at room temperature, as this reduces the efficiency of

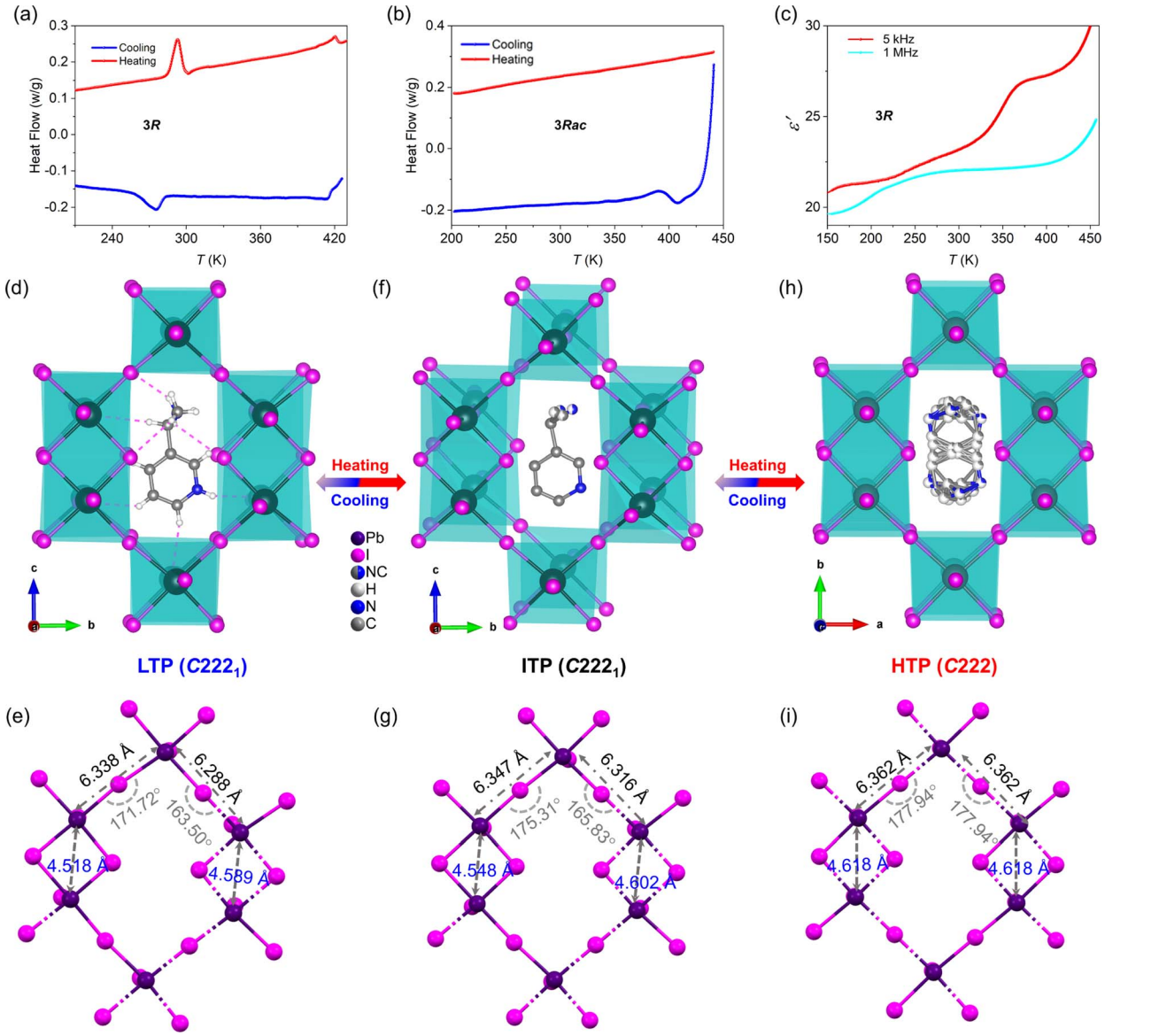


Fig. 2 (a) DSC curves of **3*R***. (b) DSC curves of **3*Rac***. (c) Dielectric transition of **3*R***. Crystal structure of **3*R*** in the ordered LTP (d), and disordered ITP (f), HTP (h) and the corresponding connection motifs (e, g, and i).

chiral transfer from the chiral cations to the inorganic framework,[48] thereby reducing the $g_{Iph}$. Although the chiral optical properties of our materials are still unsatisfactory due to the disorder of the cations, it can be foreseen that the introduction of room-temperature ordered chiral cations into 3D lead iodide structures will greatly improve the chiroptical properties of such materials. In addition to the CPL sensing, the device also exhibits good photoresponses. The $I_{ph}/I_{dark}$ ratio at 565 nm was obtained by measuring the *I*–*V* curves in the dark and under different illumination intensities from 0–0.17 mW cm$^{-2}$ (Fig. 4e). The measured responsivity and specific detectivity without frequency modulation are 0.25 A W$^{-1}$ and 3.2 × 10$^{12}$ jones, respectively (Fig. 4f). These merits indicate that the single-crystal device is a good candidate for CPL detection.

The combination of heavy element Pb and non-centrosymmetric structures (chirality) leads to the Rashba–Dresselhaus (RD) spin splitting effect. The possible existence of RD spin splitting is verified by first-principles calculation. As shown in Fig. 5a and b, band splitting occurs at the *Y* point at the base of the conduction band (Fig. 5b). The RD splitting coefficient is defined as $\alpha_{RD} = 2E_{RD}/\Delta k$, where $E_{RD}$ is the energy splitting and $\Delta k$ is the momentum shift. Fig. 5b shows that the $E_{RD}$ along the *Γ*–*Y* path is 3 meV, the $\Delta k$ is 0.0285 Å$^{-1}$, and the $\alpha_{RD}$ of the CBM is 0.21 eV Å. The $E_{RD}$ along the *Y*–$C_0$ path is 0.5 meV, the $\Delta k$ is 0.00424 Å$^{-1}$, and the $\alpha_{RD}$ of the CBM is 0.23 eV Å, which is smaller than that of 2D chiral ferroelectric (*R*-3AMP)$PbBr_4$ [22] and comparable to that of the polar quasi-2D lead iodide hybrid $(IBA)_2(EA)_2Pb_3I_{10}$ (IBA = 4-isopropylbenzylammonium, EA = ethylammonium).[49] Due to the different contributions of Pb and I elements to the CBM and

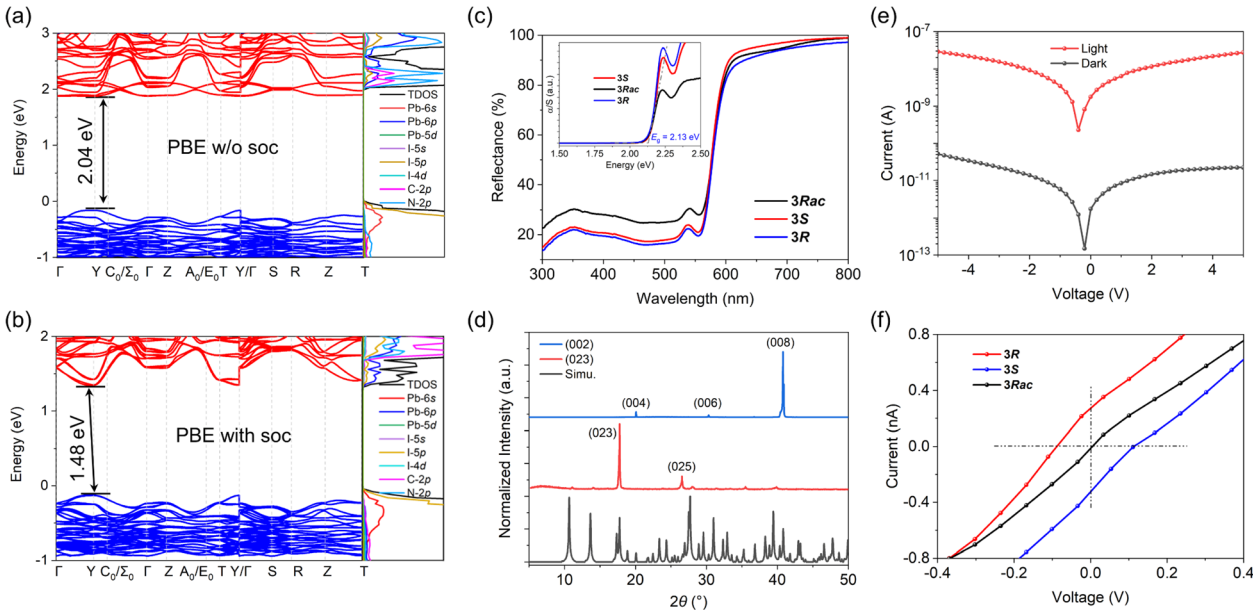


Fig. 3 (a) DFT-PBE and (b) DFT-PBE + SOC band structures and projected density of states (PDOS) of **3*R***. (c) UV-vis diffuse-reflectance spectra of **3*R*/*S*/*Rac***. Inset: optical bandgap derived from the Kubelka–Munk function based on diffuse-reflectance data. (d) PXRD patterns of the single crystal were recorded from the (023) and (001) planes. (e) *I*–*V* curves recorded in the dark and under 100 mW cm$^{-2}$ illumination along the [100]. (f) Bulk photovoltaic effect of **3*R*/*S***.

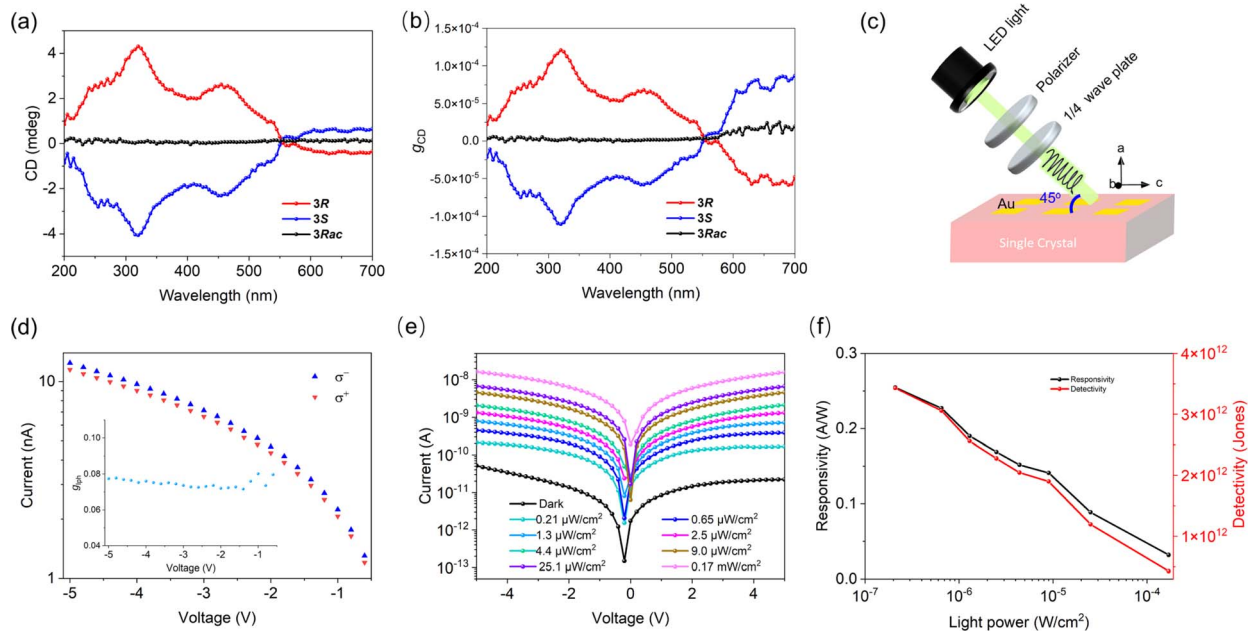


Fig. 4 (a) CD and (b) $g_{CD}$ spectra of **3*R*/*S*** and **3*R*ac**. (c) Device architecture for the CPL detection of **3*R***. (d) *I*–*V* curves of the **3*R*** photodetector under R-CPL and L-CPL illumination at 565 nm with an intensity of 0.17 mW cm$^{-2}$, as well as the calculated $g_{lph}$. (e) *I*–*V* curves under different illumination intensities at 565 nm; (f) power intensity dependence of *R* and *D** at 565 nm.

VBM, the $\alpha_{RD}$ of the VBM is much less obvious than that of the CBM (about 0.04 eV Å). The difference in $\alpha_{RD}$ values along the $\Gamma$–$Y$ and $Y$–$C_0$ paths indicates the anisotropy of the band splitting (Fig. 5b). The calculated RD effect was also verified by CPL excited photoluminescence measurements.[50] The opposite fluorescence intensity difference between **3*R*** and **3*S*** under the excitation of CPL with different helicity further indicates that the existence of RD splitting causes them to produce spin splitting bands with opposite optical helicity (Fig. S11†).

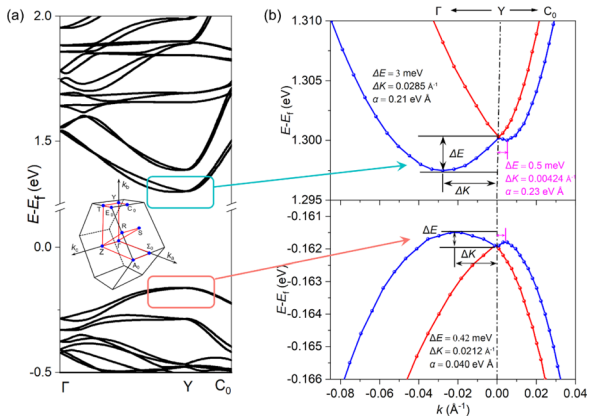


Fig. 5 (a) DFT-PBE + SOC band structure of **3*R*** along selected *k* paths (inset is the Brillouin zone with high symmetry *k* points). (b) Rashba–Dresselhaus splitting.

## Conclusions

In conclusion, we have constructed two pairs of 3D chiral lead-iodide hybrids (*R*/*S*-3AEP)$Pb_2I_6$ and (*R*/*S*-2AEP)$Pb_2I_6$ through chiral introduction and *ortho* substitution strategies and obtained bulk single crystals of **3*R*/*S***. These 3D CHMHs exhibit good circular dichroism, CPL detection performance, and the RD effect. Meanwhile, the crystal device shows excellent photodetection performances in terms of the on/off ratio, responsivity, detectivity, and bulk photovoltaic effect for self-power detection. This provides new research ideas and materials for the research and development of chiroptics and spintronics.

## Data availability

The data supporting this article have been included as part of the ESI.†

## Author contributions

Chang-Chun Fan: conceptualization, data curation, formal analysis, investigation, methodology, validation and writing-original draft; Cheng-Dong Liu: data curation and methodology; Bei-Dou Liang: visualization and formal analysis; Tong-Yu Ju supervision; Wei Wang: investigation; Ming-Liang Jin: formal analysis; Chao-Yang Chai: supervision; Wen Zhang: conceptualization, data curation, funding acquisition, resources, supervision, software and writing-review & editing.

## Conflicts of interest

There are no conflicts to declare.

## Acknowledgements

This research was made possible as a result of a generous grant from the National Natural Science Foundation of China (Grant 21991144). We thank the Big Data Center of Southeast University for providing the facility support on the numerical calculations.

## References

1 M. Liu, L. Zhang and T. Wang, *Chem. Rev.*, 2015, **115**, 7304–7397.
2 L. Guankui, Z. Yecheng, Z. Mingtao, S. Randy, R. Abdullah, H. Li, L. Girish and G. Weibo, *Adv. Mater.*, 2019, **31**, 1807628.
3 P. Duan, H. Cao, L. Zhang and M. Liu, *Soft Matter*, 2014, **10**, 5428–5448.
4 S. Ma, J. Ahn and J. Moon, *Adv. Mater.*, 2021, **33**, 2005760.
5 G. Long, R. Sabatini, M. I. Saidaminov, G. Lakhwani, A. Rasmita, X. Liu, E. H. Sargent and W. Gao, *Nat. Rev. Mater.*, 2020, **5**, 423–439.
6 H.-Y. Liu, H.-Y. Zhang, X.-G. Chen and R.-G. Xiong, *J. Am. Chem. Soc.*, 2020, **142**, 15205–15218.
7 X. B. Han, C. Y. Chai, M. L. Jin, C. C. Fan and W. Zhang, *Adv. Opt. Mater.*, 2023, **11**, 2300580.
8 J. Ahn, E. Lee, J. Tan, W. Yang, B. Kim and J. Moon, *Mater. Horiz.*, 2017, **4**, 851–856.
9 C. Y. Chai, X. B. Han, C. D. Liu, C. C. Fan, B. D. Liang and W. Zhang, *J. Phys. Chem. Lett.*, 2023, **14**, 4063–4070.
10 P. J. Huang, K. Taniguchi and H. Miyasaka, *J. Am. Chem. Soc.*, 2019, **141**, 14520–14523.
11 B.-D. Liang, C.-C. Fan, C.-D. Liu, T.-Y. Ju, C.-Y. Chai, X.-B. Han and W. Zhang, *Inorg. Chem. Front.*, 2023, **10**, 5035–5043.
12 P.-J. Huang, K. Taniguchi, M. Shigefuji, T. Kobayashi, M. Matsubara, T. Sasagawa, H. Sato and H. Miyasaka, *Adv. Mater.*, 2021, **33**, 2008611.
13 C. Yuan, X. Li, S. Semin, Y. Feng, T. Rasing and J. Xu, *Nano Lett.*, 2018, **18**, 5411–5417.
14 D. Fu, J. Xin, Y. He, S. Wu, X. Zhang, X. M. Zhang and J. Luo, *Angew. Chem., Int. Ed.*, 2021, **60**, 20021–20026.
15 C.-C. Fan, C.-D. Liu, B.-D. Liang, W. Wang, M.-L. Jin, C.-Y. Chai, C.-Q. Jing, T.-Y. Ju, X.-B. Han and W. Zhang, *Nat. Commun.*, 2024, **15**, 1464.
16 C.-K. Yang, W.-N. Chen, Y.-T. Ding, J. Wang, Y. Rao, W.-Q. Liao, Y.-Y. Tang, P.-F. Li, Z.-X. Wang and R.-G. Xiong, *Adv. Mater.*, 2019, **31**, 1808088.
17 J. Naciri, D. K. Shenoy, P. Keller, S. Gray, K. Crandall and R. Shashidhar, *Chem. Mater.*, 2002, **14**, 5134–5139.
18 H. Y. Zhang, Y. Y. Tang, P. P. Shi and R. G. Xiong, *Acc. Chem. Res.*, 2019, **52**, 1928–1938.
19 S. Jiao, H. Jiang, C. Fan, C. Xu, J. Jiang, Y. Xu, Z. Tang, X. Sun, P. Ji, X. Yang, K. Ye, L. Xu, Q. You, S. Chen, H.-L. Cai and X. Wu, *Chem. Eng. J.*, 2023, **477**, 146805.
20 T. Y. Ju, C. C. Fan, B. D. Liang, C. D. Liu, M. L. Jin, C. Y. Chai and W. Zhang, *Adv. Funct. Mater.*, 2024, **34**, 2316747.
21 K. Ishizaka, M. S. Bahramy, H. Murakawa, M. Sakano, T. Shimojima, T. Sonobe, K. Koizumi, S. Shin, H. Miyahara, A. Kimura, K. Miyamoto, T. Okuda, H. Namatame, M. Taniguchi, R. Arita, N. Nagaosa, K. Kobayashi, Y. Murakami, R. Kumai, Y. Kaneko, Y. Onose and Y. Tokura, *Nat. Mater.*, 2011, **10**, 521–526.

22 C. C. Fan, X. B. Han, B. D. Liang, C. Shi, L. P. Miao, C. Y. Chai, C. D. Liu, Q. Ye and W. Zhang, *Adv. Mater.*, 2022, **34**, 2204119.
23 D. S. Sanchez, I. Belopolski, T. A. Cochran, X. Xu, J.-X. Yin, G. Chang, W. Xie, K. Manna, V. Süß, C.-Y. Huang, N. Alidoust, D. Multer, S. S. Zhang, N. Shumiya, X. Wang, G.-Q. Wang, T.-R. Chang, C. Felser, S.-Y. Xu, S. Jia, H. Lin and M. Z. Hasan, *Nature*, 2019, **567**, 500–505.
24 S. D. Stranks, G. E. Eperon, G. Grancini, C. Menelaou, M. J. P. Alcocer, T. Leijtens, L. M. Herz, A. Petrozza and H. J. Snaith, *Science*, 2013, **342**, 341–344.
25 G. Xing, N. Mathews, S. Sun, S. S. Lim, Y. M. Lam, M. Grätzel, S. Mhaisalkar and T. C. Sum, *Science*, 2013, **342**, 344–347.
26 Q. Dong, Y. Fang, Y. Shao, P. Mulligan, J. Qiu, L. Cao and J. Huang, *Science*, 2015, **347**, 967–970.
27 W. Wang, C.-D. Liu, C.-C. Fan, X.-B. Fu, C.-Q. Jing, M.-L. Jin, Y.-M. You and W. Zhang, *J. Am. Chem. Soc.*, 2024, **146**, 9272–9284.
28 L. M. Herz, *ACS Energy Lett.*, 2017, **2**, 1539–1548.
29 J. Lim, M. T. Hörantner, N. Sakai, J. M. Ball, S. Mahesh, N. K. Noel, Y.-H. Lin, J. B. Patel, D. P. McMeekin, M. B. Johnston, B. Wenger and H. J. Snaith, *Energy Environ. Sci.*, 2019, **12**, 169–176.
30 H. Zhu, Y. Fu, F. Meng, X. Wu, Z. Gong, Q. Ding, M. V. Gustafsson, M. T. Trinh, S. Jin and X. Y. Zhu, *Nat. Mater.*, 2015, **14**, 636–642.
31 D. Shi, V. Adinolfi, R. Comin, M. Yuan, E. Alarousu, A. Buin, Y. Chen, S. Hoogland, A. Rothenberger, K. Katsiev, Y. Losovyj, X. Zhang, P. A. Dowben, O. F. Mohammed, E. H. Sargent and O. M. Bakr, *Science*, 2015, **347**, 519–522.
32 NREL, 2023, **https://www.nrel.gov/pv/cell-efficiency.html**.
33 G. Long, C. Jiang, R. Sabatini, Z. Yang, M. Wei, L. N. Quan, Q. Liang, A. Rasmita, M. Askerka, G. Walters, X. Gong, J. Xing, X. Wen, R. Quintero-Bermudez, H. Yuan, G. Xing, X. R. Wang, D. Song, O. Voznyy, M. Zhang, S. Hoogland, W. Gao, Q. Xiong and E. H. Sargent, *Nat. Photonics*, 2018, **12**, 528–533.
34 X. Wang, Y. Wang, W. Gao, L. Song, C. Ran, Y. Chen and W. Huang, *Adv. Mater.*, 2021, **33**, 2003615.
35 A. Abherve, N. Mercier, A. Kumar, T. K. Das, J. Even, C. Katan and M. Kepenekian, *Adv. Mater.*, 2023, **35**, 2305784.
36 C. Chen, L. Gao, W. Gao, C. Ge, X. Du, Z. Li, Y. Yang, G. Niu and J. Tang, *Nat. Commun.*, 2019, **10**, 1927.
37 J. X. Gao, W. Y. Zhang, Z. G. Wu, Y. X. Zheng and D. W. Fu, *J. Am. Chem. Soc.*, 2020, **142**, 4756–4761.
38 Q. Guan, T. Zhu, Z. K. Zhu, H. Ye, S. You, P. Xu, J. Wu, X. Niu, C. Zhang, X. Liu and J. Luo, *Angew. Chem., Int. Ed.*, 2023, **62**, e202307034.
39 X. Li, Y. He, M. Kepenekian, P. Guo, W. Ke, J. Even, C. Katan, C. C. Stoumpos, R. D. Schaller and M. G. Kanatzidis, *J. Am. Chem. Soc.*, 2020, **142**, 6625–6637.
40 D. Umeyama, L. Leppert, B. A. Connor, M. A. Manumpil, J. B. Neaton and H. I. Karunadasa, *Angew. Chem., Int. Ed.*, 2020, **59**, 19087–19094.
41 C.-C. Fan, B.-D. Liang, C.-D. Liu, C.-Y. Chai, X.-B. Han and W. Zhang, *Inorg. Chem. Front.*, 2022, **9**, 6404–6411.
42 J. Even, L. Pedesseau, J.-M. Jancu and C. Katan, *J. Phys. Chem. Lett.*, 2013, **4**, 2999–3005.
43 H.-Y. Zu, C.-C. Fan, C.-D. Liu, C.-Q. Jing, C.-Y. Chai, B.-D. Liang, X.-B. Han and W. Zhang, *Chem. Mater.*, 2023, **35**, 5854–5863.
44 C.-C. Fan, C.-D. Liu, B.-D. Liang, M.-L. Jin, T.-Y. Ju, C.-Y. Chai, X.-B. Han and W. Zhang, *Inorg. Chem.*, 2023, **62**, 12634–12638.
45 I. Spanopoulos, I. Hadar, W. Ke, Q. Tu, M. Chen, H. Tsai, Y. He, G. Shekhawat, V. P. Dravid, M. R. Wasielewski, A. D. Mohite, C. C. Stoumpos and M. G. Kanatzidis, *J. Am. Chem. Soc.*, 2019, **141**, 5518–5534.
46 Y. Liu, Z. Yang, D. Cui, X. Ren, J. Sun, X. Liu, J. Zhang, Q. Wei, H. Fan, F. Yu, X. Zhang, C. Zhao and S. F. Liu, *Adv. Mater.*, 2015, **27**, 5176–5183.
47 Y. Peng, X. Liu, L. Li, Y. Yao, H. Ye, X. Shang, X. Chen and J. Luo, *J. Am. Chem. Soc.*, 2021, **143**, 14077–14082.
48 M. K. Jana, R. Song, H. Liu, D. R. Khanal, S. M. Janke, R. Zhao, C. Liu, Z. V. Vardeny, V. Blum and D. B. Mitzi, *Nat. Commun.*, 2020, **11**, 4699.
49 Y. Chen, L. Tang, X. Zeng, W. Guo, T. Yang, H. Xu, Y. Liu, G. Gou, Y. Zhao, J. Luo and Z. Sun, *Adv. Funct. Mater.*, 2024, **34**, 2311726.
50 E. Lafalce, E. Amerling, Z. G. Yu, P. C. Sercel, L. Whittaker-Brooks and Z. V. Vardeny, *Nat. Commun.*, 2022, **13**, 483.